Volume 14
Number 41
7 November 2022
Pages 15205-15546

# Nanoscale

rsc.li/nanoscale

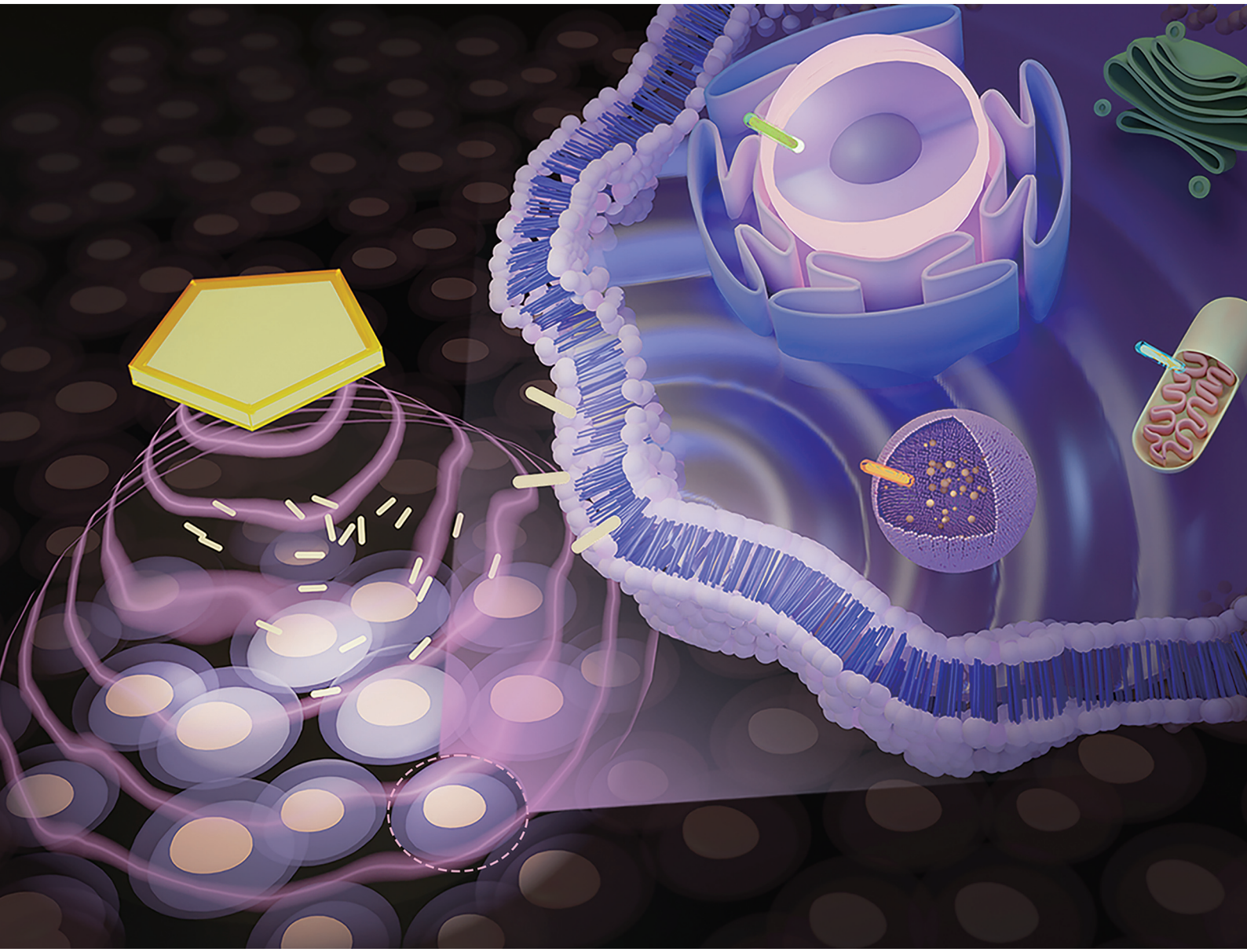

ISSN 2040-3372

ROYAL SOCIETY OF CHEMISTRY

**PAPER**
Yanyan Wang *et al.*
A targeted hydrodynamic gold nanorod delivery system based on gigahertz acoustic streaming

NCNST

Nanoscale

PAPER

View Article Online
View Journal | View Issue



Cite this: *Nanoscale*, 2022, **14**, 15281

# A targeted hydrodynamic gold nanorod delivery system based on gigahertz acoustic streaming†

Shan He, Wei Pang, Xiaoyu Wu, Yang Yang, Wenjun Li, Hang Qi, Chongling Sun, Xuexin Duan and Yanyan Wang *

The hydrodynamic method mimics the *in vivo* environment of the mechanical effect on cell stimulation, which not only modulates cell physiology but also shows excellent intracellular delivery ability. Herein, a hydrodynamic intracellular delivery system based on the gigahertz acoustic streaming (AS) effect is proposed, which presents powerful targeted delivery capabilities with high efficiency and universality. Results indicate that the range of cells with AuNR introduction is related to that of AS, enabling a tunable delivery range due to the adjustability of the AS radius. Moreover, with the assistance of AS, the organelle localization delivery of AuNRs with different modifications is enhanced. AuNRs@RGD is inclined to accumulate in the nucleus, while AuNRs@BSA tend to enter the mitochondria and AuNRs@$PEG_{nK}$ tend to accumulate in the lysosome. Finally, the photothermal effect is proved based on the large quantities of AuNRs introduced *via* AS. The abundant introduction of AuNRs under the action of AS can achieve rapid cell heating with the irradiation of a 785 nm laser, which has great potential in shortening the treatment cycle of photothermal therapy (PTT). Thereby, an efficient hydrodynamic technology in AuNR introduction based on AS has been demonstrated. The outstanding location delivery and organelle targeting of this method provides a new idea for precise medical treatment.

Received 11th June 2022,
Accepted 5th September 2022

DOI: 10.1039/d2nr03222h

rsc.li/nanoscale



## 1. Introduction

A hydrodynamic system based on fluid shear force is widely applied in the intracellular delivery of different kinds of substances.[1] Such fluid shear force can induce membrane poration by the deformation or temporary disruption of cells with less invasiveness and excellent biocompatibility.[2] Meanwhile, the ability of fluids in cell poration can be adjusted by fluid flow patterns or shear force levels, which was typically regulated with microstructure or acoustic intensity.[3] In microchannel systems, shear forces are generated by fluid velocity gradients caused by different microstructural restrictions, which can enhance the cell membrane permeability.[4] As a spiral vortex is generated in the cross- or T-junction sites, the permeability of the cell membrane changed with the cell deformation and the highly effective intracellular delivery of large nanomaterials was achieved.[5,6] Even better, the hydrodynamic system based on microfluidics is able to realize the delivery of external substances without affecting the later culture and characterization of cells.[7] However, the fluid shear force levels will be determined with the microstructure, which limits its adjustability.[8]

The hydrodynamic poration method based on the acoustic wave optimizes the adjustability of the intracellular delivery system, of which the fluid shear force acted on cells is realized through the conversion of acoustic energy to liquid kinetic energy. Continuous adjustment of the shear force can be achieved by changing the acoustic input energy, which simplified the experimental process. There are two categories of acoustic-based intracellular delivery methods: bubble-based sonoporation and non-bubble-based sonoporation. Bubble-based sonoporation typically relies on ultrasound-induced bubble cavitation.[9] The cavitation can trigger drug delivery through mechanisms of thermal, chemical and mechanical effects. The thermal effect relies on the acoustic radiation from oscillating bubbles, which is able to heat the surroundings, thus promoting the drug release from thermally sensitive carriers.[10] The chemical effect relies on the temperature rise inside the bubble caused by acoustic energy, which is more obvious than the surroundings. This extreme heat condition is only sustained for a brief period (<1 μs), but can lead to the emission of electromagnetic radiation and production of highly reactive chemical species, to further activate certain types of drugs without degradation.[11] The mechanical effect relies on the volumetric oscillations of bubbles that are exposed to an ultrasound field, which is sufficient to impose

*State Key Laboratory of Precision Measuring Technology and Instruments, College of Precision Instruments and Opto-electronics Engineering, Tianjin University, Tianjin 300072, China. E-mail: yanyanwang@tju.edu.cn*

† Electronic supplementary information (ESI) available. See DOI: https://doi.org/10.1039/d2nr03222h

substantial forces on nearby surfaces and promote drug release from particles.[12] Additionally, microstreaming generated by the oscillating bubbles[13] and liquid microjetting generated with the bubble collapse[14] have been demonstrated such that the fluid force applied on nearby cells can promote intracellular drug delivery.

The non-bubble-based sonoporation method was recently developed, which reduced the system instability and complexity caused by bubbles. Non-bubble-based sonoporation typically relies on the acoustic radiation force and shear force induced by acoustic streaming (AS).[15] Acoustic radiation force dominates cell poration and intracellular delivery at acoustic frequencies ranging from kilohertz to megahertz. Bulk acoustic wave (BAW) and surface acoustic wave (SAW) are two common wave modes in sonoporation. Based on the BAW generated by the piezoelectric transducer, the acoustic radiation force is able to induce dextran (500 kDa) intracellular delivery to several cells.[16] BAW can not only achieve efficient substance delivery, but its accuracy of intracellular delivery can also be improved by the range of BAW. As the developed piezoelectric micropillars, localized sonoporation can be achieved of the target cell in small areas above the micropillars.[17] Based on the SAW generated by the interdigitated transducer, the acoustic radiation force is able to change the permeability of the cell membrane, which is attached to a solid substrate and achieves acoustically-mediated intracellular delivery.[18] Similarly, the precisely control of the range of drug delivery can also be realized with the area of SAW, as a narrowly focused SAW can be generated by changing the structure of the interdigital electrode.[19]

With the frequency of an acoustic wave up to the gigahertz range, the shear force induced by acoustic streaming dominates cell poration.[20] In our previous works, the acoustic streaming excited by a gigahertz bulk acoustic resonator was able to exert a shear force on the cell membrane, and induce cell deformation together with the change of the cell membrane permeability, which was confirmed by the intracellular delivery of doxorubicin hydrochloride (DOX).[21] In addition, this hydrodynamic delivery system based on gigahertz AS has been proved to promote plasmid,[22] biologically active proteins[23] and even drug-loaded mesoporous silica nanoparticles,[24] which provides a novel method for the intracellular delivery of substances with different properties.

Nanomaterials exhibit superiority in cellular imaging, drug delivery and cell therapy due to their excellent physical and chemical performances.[25] Among many nanomaterials, gold nanorods (AuNRs) show great prospects for extensive application in cell biology. It can be used as a drug carrier to achieve intracellular drug delivery due to the ease of synthesis and modification.[26] Meanwhile, AuNRs display great optical absorbance[27] and scattering enhancement[28] based on surface plasmon resonance, making them ideal contrast agents in a number of applications, such as photothermal therapy (PTT),[29,30] photoacoustic imaging (PAI)[31,32] and dark-field imaging.[33] At present, the main way to achieve bulk delivery of AuNRs is the coincubation method based on endocytosis. This makes the delivery duration last for several hours to days,[34,35] reducing the application efficiency of AuNRs. Therefore, it is an urgent issue to improve the implementation efficiency caused by long-term introduction.

Herein, a hydrodynamic delivery system of AuNRs based on the gigahertz AS effect is proposed. We demonstrate that the intracellular delivery of AuNRs can only be realized in the range of AS, revealing the cell location property of AS intracellular delivery. The delivery efficiency of AS stimulation compared with that of the coincubation method is tested, which prove the rapid intracellular delivery of AuNRs, regardless of the different surface modifications of AuNRs or different cell lines. By calculating the colocalization coefficient, we identify the preference of AuNRs with different modifications into different organelles under AS action—that AuNRs@RGD is inclined to the nucleus, AuNRs@BSA tends to prefer the mitochondria and AuNRs@PEG$_{nK}$ prefers the lysosome. Finally, we demonstrate that the photothermal effect relies on the rapid intracellular introduction of AuNRs in large quantities. Cells can heat up rapidly with 785 nm laser irradiation according to the plasmonic resonant optical absorbance of AuNRs, which effectively shortens the cycle of photothermal therapy. Thus, the efficient and unrestricted delivery of AuNRs with AS stimulation has been proved. Meanwhile, cell location and organelle-guided AuNR delivery imply promising prospect in precision medicine.

## 2. Results and discussion

### 2.1 Rapid intracellular delivery of AuNRs

AuNRs were synthesized using the seed-mediated growth method[36,37] and functionalized by five kinds of molecules (Fig. 1A), including thiolated polyethylene glycol with fluor-

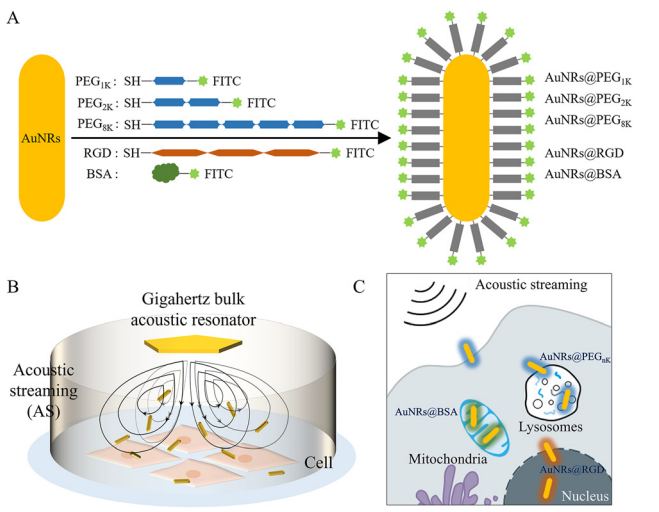


Fig. 1 A. Schematic diagram of AuNRs modified with five different molecules. B. Schematic illustration of the AS-induced AuNR delivery. C. The fluid shear force generated by AS causes cell membrane permeability changes and enhances the AuNR entry to different organelles.

escein isothiocyanate (SH-PEG-FITC) with three different molecular weights (8K, 2K and 1K), thiolated arginine-glycine-aspartic acid with fluorescein isothiocyanate (RGD-FITC), and bovine serum albumin with fluorescein isothiocyanate (BSA-FITC). To verify the modification of different molecules, the zeta potential, hydrodynamic diameter and fluorescence intensity of the modified AuNRs were characterized. The reduced zeta potentials (Fig. S1A†), increased hydrodynamic diameters (Fig. S1B†), and enhanced fluorescence luminescence intensity (Fig. S1C†) of the modified AuNRs indicated that these five molecules are successfully modified on the surface of AuNRs, thus altering the surface charge, size and fluorescence property. To further characterize the modification of AuNRs and their imaging ability in the fluorescence field, the location of the modified AuNRs in fluorescence and the reflection field are also imaged. As shown in Fig. S1D,† it was found that modified AuNRs can be co-located in fluorescence field (green color, FITC related molecules) and reflection field (glow color, AuNRs). Not only does this indicate the successful modification of molecules but it also proves the feasibility of using a fluorescence field to determine the location of AuNRs.

After successful functionalization, the intracellular delivery of AuNRs excited with AS were investigated as follows. The hydrodynamic AuNR delivery system based on the AS effect is illustrated as Fig. 1B. The resonator is placed on the opposite side of the coverslip from where the cells are cultured. The polydimethylsiloxane (PDMS) chamber in the middle is used to control the cells 0.5 mm away from the resonator and contains AuNR solution. The resonator vibrates and produces an acoustic wave with 1.58 GHz when a sinusoidal electrical signal is input. With the attenuation of the acoustic wave travelling through the liquid, the AS effect is generated.[38,39] When the AS encounters an interfacial obstruction, its velocity and direction will be altered, and then the shear force is generated on the interface. The fluid shear force of AS causes cell deformation and membrane permeability changes, promoting the entry of AuNRs into cells or even different organelles (Fig. 1C).

In the following experiment, the delivery range of AuNRs with AS stimulation was explored. HeLa cells were exposed to AS and AuNRs@RGD for 10 minutes. As shown in Fig. 2A, the yellow circle indicates the PDMS chamber and the blue fluorescence of the nucleus is used for cell localization within the chamber. Cells showing green fluorescence indicate the introduction of AuNRs@RGD. The white circle represents the range of cell that achieved AuNRs@RGD introduction. To determine the range of AuNR delivery with AS action, the fluorescence intensity of cells at green and red lines were measured with Fiji (these two paths were selected due to the higher quantity of cells on the line) and shown in Fig. 2B and C respectively. Every blue fluorescent peak represents a cell. The overlap of both green and blue fluorescence peaks indicates that AuNRs@RGD have entered cell. All cells show uniform blue fluorescence distribution without any location difference, while only localized cells show green fluorescence representing AuNRs@RGD intracellular introduction. The distribution

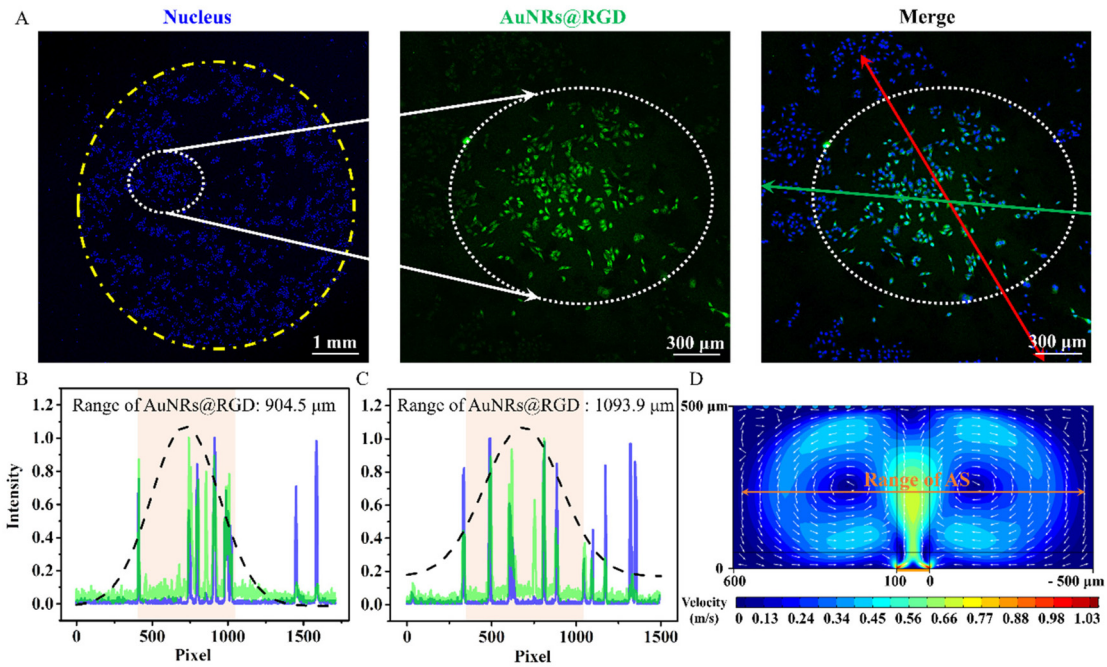


Fig. 2 A. The fluorescence images of the nuclei of all HeLa cells and AuNRs@RGD delivered cells. The yellow circle represents the range of the PDMS chamber, the white circle represents the range of cells that are delivered by AuNRs@RGD. B. The normalized fluorescence intensity of cells on the green line. C. The normalized fluorescence intensity of cells on the red line. Blue line: the intensity of nucleus, green line: the intensity of AuNRs@RGD, black line: the Gaussian fit of the intensity of AuNRs@RGD. D. 2D finite element simulation (FEM) of AS generated by resonator with input power of 500 mW and height of 0.5 mm. The white arrows in the image represent the direction of the AS.

range of green fluorescence (orange area in Fig. 2B and C) on green and red lines are calculated as 904.5 μm and 1093.9 μm, respectively. The AS was simulated with an input power of 500 mW and height of 0.5 mm, and the range of AS is simulated around 1000 μm (Fig. 2D), which is consistent with the range of cells realized AuNRs@RGD introduction, indicated that the AuNR intracellular delivery can be achieved by the AS method and the delivery range is related to that of AS. Depending on the advantages of tunable of AS range (by adjusting the input power of resonator and height between cells and resonator[38]), the AuNRs intracellular delivery can also achieve range regulation.

To further characterize the AuNRs intracellular importation and accumulation process with 10 min AS stimulation, the changes of cell fluorescence over time was monitored. As shown in Fig. S2A,† when power is applied on the resonator, AS is created and stimulated the AuNRs@$PEG_{1K}$ entering the cytoplasm immediately. Over time, more AuNRs@$PEG_{1K}$ enter the cells, which mainly distribute throughout the cytoplasm (Fig. 3A). This phenomenon is also confirmed with the Z-stack images (Fig. 3B). From the bottom of the cell to the top, AuNRs@$PEG_{1K}$ can be observed in the cytoplasm at different layers. These results indicate that AS is capable of realizing the AuNRs@$PEG_{1K}$ intracellular delivery within 10 min. To further verify the ability of AS to promote the intracellular delivery of AuNRs with different surface properties, the other four functionalized AuNRs, as AuNRs@$PEG_{2K}$, AuNRs@$PEG_{8K}$, AuNRs@BSA and AuNRs@RGD were studied systematically. With 10 min AS stimulation, the green fluorescence in the cells of different AuNRs is significantly enhanced compared to the co-incubation group,[39] as shown in Fig. 3A and C. In particular, AuNRs@RGD can not only enter the cytoplasm but also nucleus, may due to the selectivity of RGD peptides to integrin, which is expressed at much higher concentrations in the nucleus of the epithelial cancer cells.[40] To clearly observe the process of AuNRs@RGD entering the nucleus, the delivery process of AuNRs@RGD is recorded and shown in Fig. S2B.† At $t$ = 0 min, the nuclei show red fluorescence, the AuNRs@RGD in the PDMS chamber show green fluorescence, and there is no fluorescence in the cytoplasm. At $t$ = 1 min, the resonator starts to work and generates AS. According to the enhancement of green fluorescence, AuNRs@RGD gradually accumulate towards the edge of cells. At $t$ = 2 min, the obvious green fluorescence of AuNR@RGD can be observed in the cytoplasm of the peripheral cell. AuNRs@RGD begin to enter the nucleus at $t$ = 3 min, and more AuNRs@RGD enter cells with

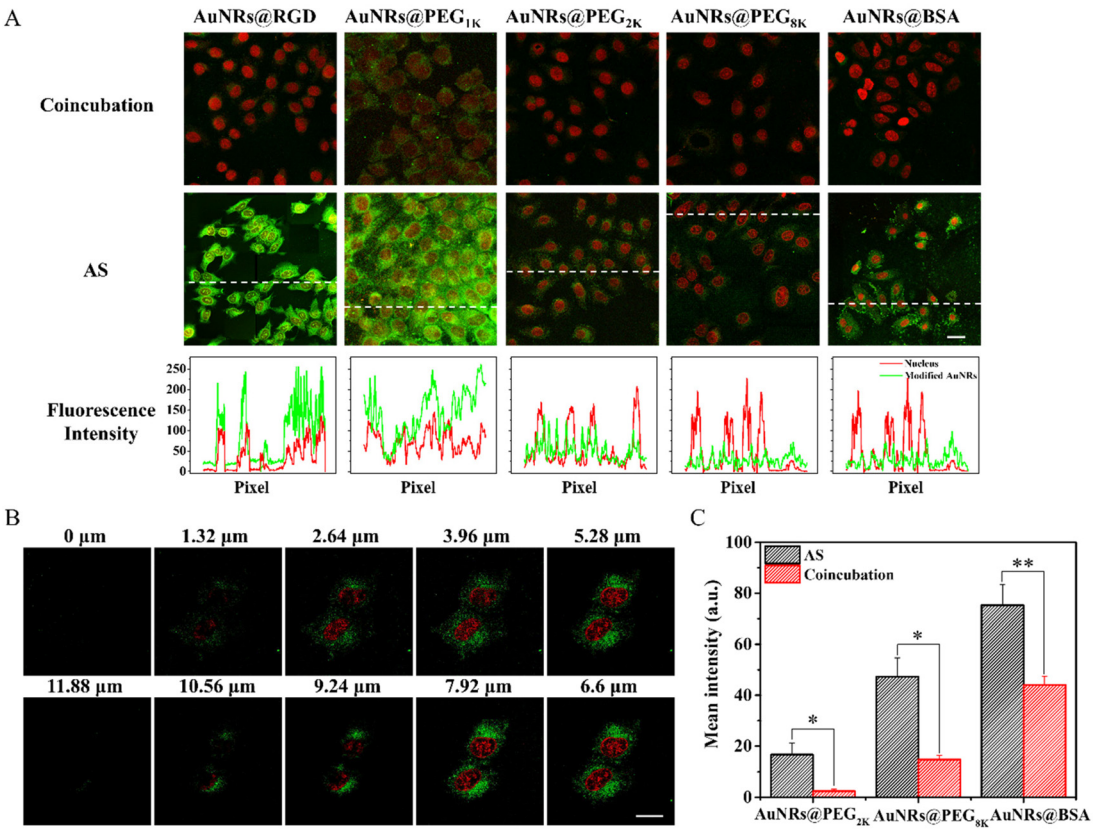


Fig. 3 A. The delivery of different modified AuNRs with coincubation and AS method with 10 minutes. Scale bar = 20 μm. The fluorescence intensities of the nucleus and AuNRs at the dotted line in the AS group are shown in the bottom line. The nuclei were stained with NucRed™ Live 647 ReadyProbes and set as red, AuNRs were set as green. B. Confocal images at different $Z$-axis values of the AS induced AuNRs@$PEG_{1K}$ cellular internalization. Scale bar = 10 μm. C. The mean intensity of different modified AuNRs with AS and coincubation method (n = 4). *p < 0.05, **p < 0.01.

the increase in the AS stimulation time. Eventually, AuNRs@RGD fill the whole cell. This phenomenon identifies the efficient and fast AuNR intracellular delivery with the assistance of AS. From the above results, it is demonstrated that this hydrodynamic system based on AS is an effective means to realize intracellular delivery and has less effect on cell viability (Fig. S3†). Compared with the co-incubation method in which the endocytosis of AuNRs into cells needs several hours to days, the introduction time with AS stimulation is reduced to less than 10 minutes.

### 2.2 Organelle target AuNRs delivery

Organelle targeted delivery enables the majority of the delivered substances to enter the target sites with reduced accumulation in other locations, playing an important role in the regulation of cell biological functions.[41] To determine the intracellular distribution of AuNRs with AS stimulation, the amount of modified AuNRs in different organelles are evaluated by the Pearson's correlation coefficient.[29] The nucleus, mitochondria and lysosomes of the cells were each labeled with fluorescent probes. After AuNRs were delivered with AS and coincubation methods, the colocalization correlation coefficient of AuNRs and organelles were calculated by Coloc 2 of Fiji. According to the correlation coefficient, the distribution of AuNRs@RGD in the lysosomes and nucleus is more obvious with the coincubation method. However, with AS stimulation, the amount of AuNRs@RGD in the mitochondria and nucleus is increased, which is more obvious in the nucleus (Fig. 4A and S4A†). Similarly, the distribution of AuNRs@BSA in the nucleus and mitochondria increases significantly with AS stimulation. The difference is that the AuNRs@BSA accumulation in mitochondria is more pronounced (Fig. 4B and S4B†). In contrast, the PEGylated AuNRs hardly enter the nucleus with AS or coincubation method (Fig. S5†). In the coincubation group, AuNRs@PEG$_{nK}$ tend to accumulate in the mitochondria and lysosomes. Under the action of AS, the colocalization correlation coefficient of AuNRs@PEG$_{nK}$ and lysosomes increase significantly, indicating that more AuNRs@PEG$_{nK}$ enter the lysosomes (Fig. 4C–E and Fig. S5†). These results suggest that although the amount of AuNRs entering the cells increase significantly with AS stimulation, the selectivity of AuNRs with different modifications to organelles is different. AuNRs@RGD is inclined to enter the nucleus and AuNRs@BSA tends to enter the mitochondria, while AuNRs@PEG$_{nK}$ prefers to enter the lysosome under AS stimulation. Compared with the coincubation method, AS not only shortens the entry time of AuNRs into the cells but also enables them to accumulate in different organelles. In the

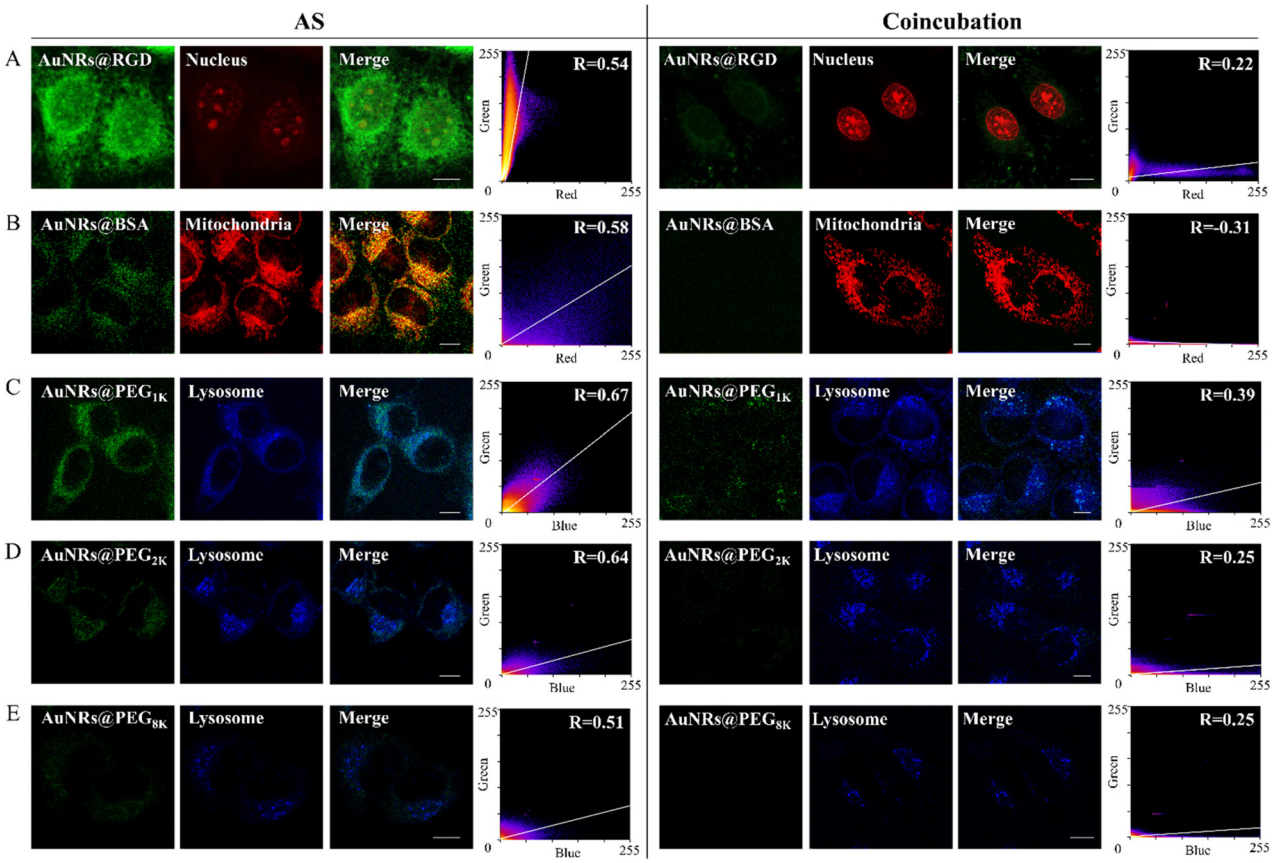


**Fig. 4** CLSM images and the Pearson's correlation coefficient for intracellular tracking after (A) AuNRs@RGD, (B) AuNRs@BSA, (C) AuNRs@PEG$_{1K}$, (D) AuNRs@PEG$_{2K}$ and (E) AuNRs@PEG$_{8K}$ delivered with AS and co-incubation method. Scale bar = 10 μm.

hydrodynamic system based on AS, AuNRs with different modifications are capable of entering different organelles, which may provide a means for targeted intracellular delivery.

### 2.3 AuNRs delivery in different cell lines

To further evaluate the AS effect on the intracellular delivery of AuNRs, two other cell lines, breast epithelial cancer cells (MCF-7) and breast epithelial healthy cells (MCF-10A) were chosen and characterized. The confocal microscope images of these two cell lines in Fig. 5 and Fig. S6† demonstrate that a higher amount of AuNRs was delivered into the cells under the AS effect compared with the coincubation group, which is consistent with the results of the HeLa cells. Moreover, both cell lines reveal that under the assistance of AS, AuNRs@$PEG_{1K}$ and AuNRs@BSA are mainly accumulated in the cytoplasm, while a great amount of AuNRs@RGD can enter the nucleus.

Compared with the cancer cell line MCF-7, the normal MCF-10A cells show a higher delivery amount of all three AuNRs (AuNRs@$PEG_{1K}$, AuNRs@BSA and AuNRs@RGD) under the assistance of acoustic streaming (Fig. 5B and Fig. S6B†). In particular, AuNRs@$PEG_{1K}$ and AuNRs@BSA exist in both cytoplasm and nucleus, which is not seen in the other two cancer cell lines. This may be caused by the selectivity of the rod-like nanoparticles of normal cells compared to cancer cells.[42–44] The introduction of AuNRs@RGD is similar to that of the AuNRs@$PEG_{1K}$ and AuNRs@BSA groups (Fig. S6B†). It can be concluded that AS is an effective means for delivery in both cancer cells and normal cells. In particular, AuNRs can also enter the nucleus with AS stimulation when there is a targeted property of AuNRs, which is hardly achieved by coincubation method in such short duration.[45]

### 2.4 Photothermal therapy

Photothermal therapy (PTT) is a therapeutic method to induce tumor cell apoptosis by artificially increasing the local temperature, taking advantage of the weak defense of cells against heat.[46] AuNRs are commonly used in photothermal therapy due to their excellent plasmonic resonant optical absorbance and photothermal conversion efficiencies. After the AuNR introduction by AS and coincubation method, cells were irradiated with a 500 mW near-infrared (NIR) light of 785 nm, and the photothermal reactions of AuNRs were recorded (Fig. S7†). As shown in Fig. 6, the temperature of the AuNR solution increases to almost 60 °C immediately with applied NIR light, demonstrating the excellent photothermal property of the modified AuNRs. The temperatures of the cells with

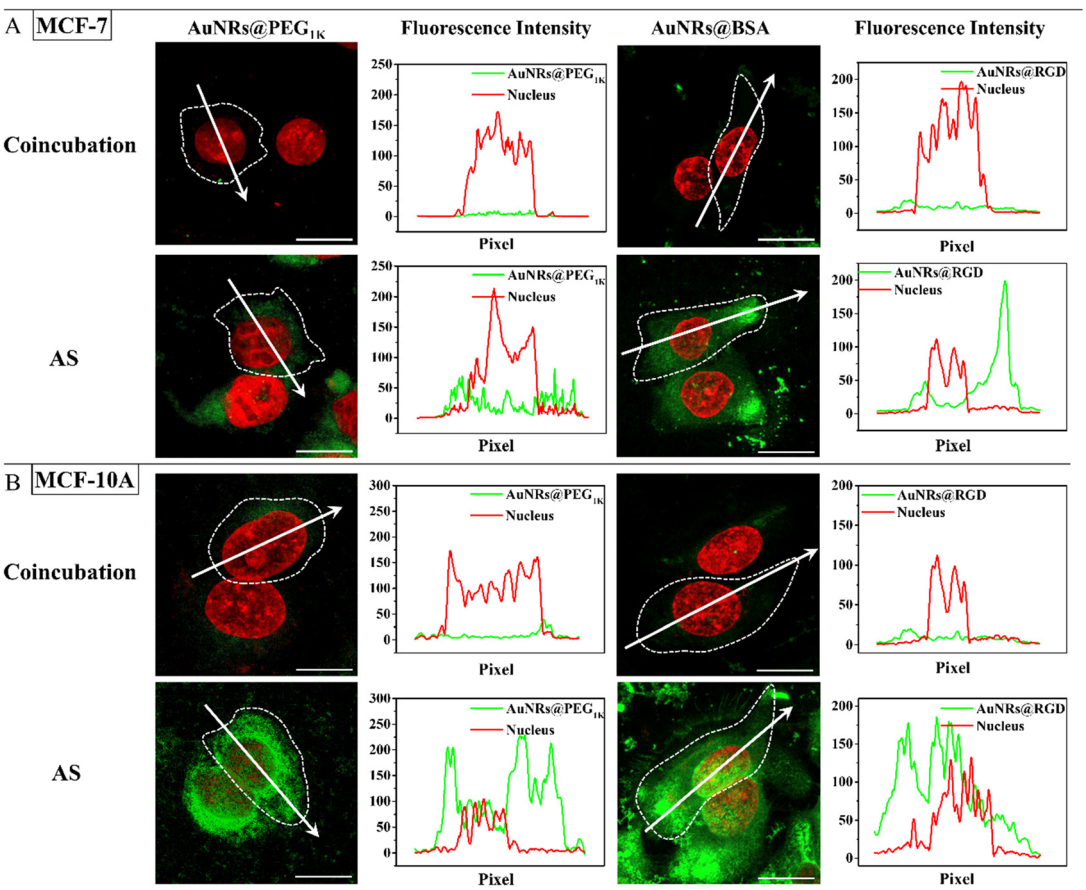


Fig. 5 A. AuNRs@$PEG_{1K}$ and AuNRs@BSA intracellular delivery of MCF-7 cells induced by AS and coincubation. B. AuNRs@$PEG_{1K}$ and AuNRs@BSA cellular delivery of MCF-10A cells induced by resonator and coincubation. The line graph represents fluorescence intensity distribution at the indicated section (white arrow). The dotted line represents the contours of the cells. Scale bar = 10 μm.

 

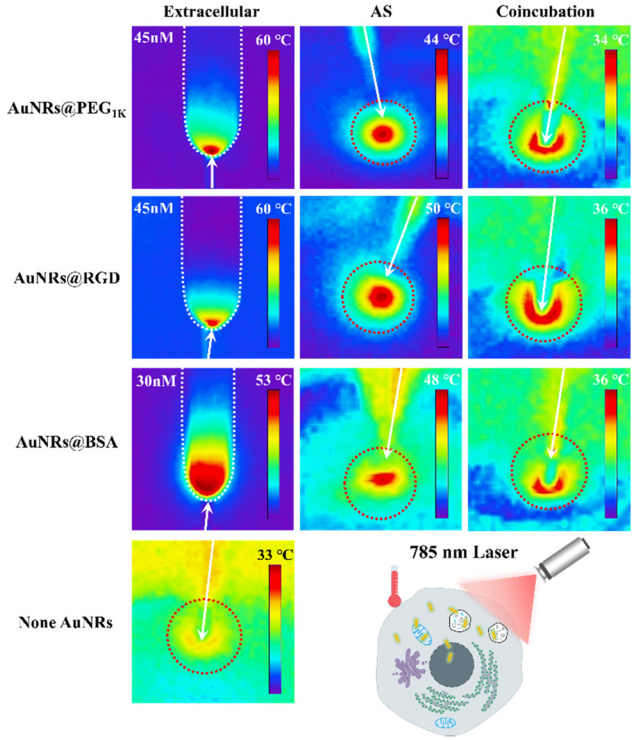


**Fig. 6** Photothermal images of intracellular and extracellular AuNRs@$PEG_{1K}$, AuNRs@RGD and AuNRs@BSA under irradiation by a NIR laser (785 nm, 500 W $cm^{-2}$) for 10 min. The white dotted line represents the centrifugal tube, the red dotted line represents the coverslip with HeLa cells, and the white arrow represents the laser beam.

AuNRs@$PEG_{1K}$, AuNRs@RGD and AuNRs@BSA introduction *via* the coincubation method are 34 °C, 36 °C and 36 °C, respectively, after irradiation with NIR light. When AuNRs@$PEG_{1K}$, AuNRs@RGD and AuNRs@BSA are delivered into the cells with AS stimulation, the temperatures rise to 44 °C, 50 °C and 48 °C *via* NIR irradiation, respectively, which increase more obviously compared with the coincubation group. With trypan blue staining (Fig. S8†), it was found that the cells with the AS-assisted delivery of AuNRs had the lowest viability after the photothermal treatment. This phenomenon further confirms that more AuNRs are delivered into cells with the acoustic streaming effect and can effectively shorten the treatment time with great potential in constructing a rapid photothermal therapy platform.

## 3. Conclusion

In summary, an efficient and targeted hydrodynamic AuNR delivery system was established based on the gigahertz AS effect. The introduction of AuNRs can only be realized within the AS action area, making the range of intracellular delivery adjustable. AS can achieve the efficient and rapid intracellular delivery for AuNRs with different surface modifications compared with the coincubation method. Furthermore, this hydrodynamic delivery method can achieve organelle-targeted introduction. Combined with different modifications, AS is able to enhance the delivery of AuNRs into different organelles, such as the nucleus, mitochondria and lysosome. In addition, the rapid and mass introduction of AuNRs induced by the AS effect can significantly shorten the period of photothermal therapy. Therefore, this hydrodynamic–AuNRs delivery system based on the AS effect not only has considerable import efficiency but also has cell location and organelle selectivity. Meanwhile, combined with the small size, easy integration and prominent CMOS (complementary metal–oxide semiconductor) compatibility, this bulk acoustic resonator has a great application potential in the field of drug release.

## 4. Experimental section

### 4.1 AuNRs modification and characterization

Gold nanorods (AuNRs) were synthesized and modified based on the previous report.[36] The bare AuNRs were modified by thiolated polyethylene glycol with fluorescein isothiocyanate (SH-PEG-FITC, Shanghai yuanye Bio-Technology) with molecular weights of 8K, 2K and 1K, thiolated arginine-glycine-aspartic acid with fluorescein isothiocyanate (RGD-FITC, NJPeptide), and bovine serum albumin with fluorescein isothiocyanate (BSA-FITC, Solarbio). Specifically, 150 μL SH-$PEG_{1K}$-FITC (5 mg $mL^{-1}$), 80 μL SH-$PEG_{2K}$-FITC (5 mg $mL^{-1}$), 30 μL SH-$PEG_{8K}$-FITC (5 mg $mL^{-1}$), 50 μL RGD-FITC (5 mg $mL^{-1}$) and 50 μL BSA-FITC (5 mg $mL^{-1}$) were added into 1 mL AuNRs (50 nM) and incubated for 8 min, 10 min, 1.5 h, 5 min and 3 min, respectively. Then, 150 μL thiolated polyethylene glycol (SH-$PEG_{1K}$) was added to the mixture and incubated for another 1 h to avoid the aggregation of AuNRs during the RGD-FITC and BSA-FITC surface modification. After incubation, excess molecules are removed by centrifugation at 3500 rpm for 3 min to terminate the reactions in the mixture.

Modified AuNRs were characterized with emission fluorescence spectra by a microplate reader (Varioskan LUX Multimode Microplate Reader, Thermofisher). The images of the modified AuNRs in fluorescence and reflective fields were observed using 63× oil lens of the confocal laser scanning microscope (CLSM, Leica SP8) with the fluorescence mode (excitation: 488 nm, emission: 500–535 nm) and reflection mode (excitation: 638 nm, emission: 700–795 nm), respectively. The changes of the zeta potential and the distribution of the particle size for different functionalized AuNRs (0.5 nM) in liquid were characterized using a Zeta Sizer (Nano ZS90, Malvern).

### 4.2 Bulk acoustic wave resonator microchip fabrication

The gigahertz bulk acoustic resonator, a solid-mounted thin-film piezoelectric resonator (SMR), was fabricated with a standard micro-electro-mechanical system (MEMS) process.[38,47] Three pairs of aluminium nitride (AlN) and silicon dioxide ($SiO_2$) used as the Bragg reflector were mounted onto the silicon substrate alternately with plasm-enhanced chemical

vapor deposition (PECVD) and reactive sputtering, respectively. Then, a molybdenum (Mo) layer was deposited onto the Bragg reflector with radio-frequency (RF) and patterned *via* plasm etching to serve as the bottom electrode. Next, the highly *c*-axis oriented AlN was deposited onto the bottom electrode as a piezoelectric layer. Finally, gold (Au) was evaporated on the top of the piezoelectric layer and patterned *via* lift-off process to use as the top electrode.

### 4.3 AS – AuNRs intracellular delivery system

The culture medium of the HeLa cells and MCF-7 cells is DMEM (Gibco) with 10% fetal bovine serum (FBS, Invitrogen). The culture medium of the MCF-10A cells is RPMI-1640 (Gibco) with 10% FBS. These cell lines were incubated in a humidified atmosphere with 37 °C and 5% $CO_2$.

For the intracellular delivery of modified AuNRs, $1 \times 10^5$ cells were seeded onto a poly-L-lysine (PLL)-coated coverslip and cultured for 24 hours. A polydimethylsiloxane (PDMS) chamber with a height of 0.5 mm was placed between the resonator and coverslip, which was filled with AuNRs (dilute to 5 nM with PBS). When the bulk acoustic resonator was stimulated with an external sinusoidal electrical signal with 1.58 GHz and 500 mW, the gigahertz acoustic wave was generated when the inverse piezoelectric effect was triggered. As the acoustic wave propagated through the liquid, the acoustic energy dissipated into the liquid and caused a body force to be driven the fluid. When the liquid was hindered by a coverslip during upward movement, the velocity would decrease to zero, thus creating a vortex-shaped fluid field (called acoustic streaming, AS), accompanied with shear force generation on the cells at the liquid–solid surface. Therefore, the cells suffered from the fluid shear force when the resonator was turned on, which promoted the AuNR intercellular delivery.

### 4.4 Characterization of the AuNR intracellular delivery

To detect the range of the AuNR delivery *via* AS, cells after AuNRs@RGD delivery induced by AS were fixed with 4% paraformaldehyde at room temperature and DAPI was used to label the cell nucleus. The CLSM was used to scan 25 fields of vision, and they were combined into one image *via* photomerging of LAS X (the software of Leica microscope). Then, Fiji software was used to calculate the diameter of the delivery region, which was obtained by calculating the number of pixels and the unit distance of each pixel.

To detect the intracellular delivery efficiency and organelle targeting of AuNRs induced by AS, organelles were labeled with immunfluorescent dyes. The AS-induced AuNR intracellular delivery was performed and cells were fixed with 4% paraformaldehyde at room temperature. Then, the cells were observed by 63× oil lens with the x-y-z mode of CLSM. The nuclei were stained with NucRed™ Live 647 ReadyProbes (Thermo Fisher Scientific) at 37 °C for 10 min, and set as a red color (excitation: 638 nm, emission: 674–690 nm). The lysosomes were stained with LysoTracker® Red DND-99 at 37 °C for 30 min (Thermo Fisher Scientific), and set as a blue color (excitation: 552 nm, emission: 585–615 nm). The mitochondria were stained with MitoTracker® Deep Red FM at 37 °C for 15 min (Thermo Fisher Scientific), and set as a red color (excitation: 638 nm, emission: 640–670 nm). The AuNRs were set as a green color (FITC, excitation: 488 nm, emission: 500–535 nm). AuNRs@$PEG_{1K}$, AuNRs@$PEG_{2K}$, AuNRs@$PEG_{8K}$ and AuNRs@BSA were images with the same parameters (Laser intensity: 9.6%, Gain 138 V). The AuNR@RGD groups were observed with 0.1% of laser intensity and 41 V of gain to avoid overexposure. The fluorescence intensity of the modified AuNRs and nucleus were measured and analyzed by Fiji. The Pearson's correlation coefficients of the co-localization evaluation were calculated by Coloc 2 in Fiji.

To record the process of AuNRs@$PEG_{1K}$ and AuNRs@RGD intracellular delivery *via* AS stimulation, the x-y-z-t mode of CLSM was used. During the total of 12 minutes recording time, the resonator was turned on at $t$ = 1 min and turned off at $t$ = 11 min. An x-y-z scan was taken per minute; the $z$-axis was set as 40 pieces.

For the photothermal therapy, cells were activated by a 500 mW near-infrared (NIR) light with a wavelength of 785 nm for 10 min, and the temperature of the cells was characterized with a thermal infrared imager (DT-980, CEM). After the PTT, cells were stained with trypan blue (dilute with PBS) and observed with an inverted microscope (Leica DMI 8).

### 4.5 Statistical analysis

All experiments were performed at least four times ($n$ = 4). The fluorescence quantitative analysis in the experiment was carried out using the Fiji software. Identical parameters of the edge extraction algorithm and denoising algorithm were utilized to analyze the same batch of fluorescence images. The average fluorescence intensity is defined as the ratio of the total fluorescence intensity of the denoised image to the area of cells.

## Author contributions

Y.W. conceived the idea and designed the experiments, S.H. performed the experiments and analyzed the results, X.W. and W.L. synthesized and modified AuNRs, H.Q. analyzed the Pearson's correlation coefficient, C.S., W.P and X.D. designed the resonator, Y.Y. executed the simulation, S.H. and Y.W. wrote the paper.

## Conflicts of interest

There are no conflicts to declare.

## Acknowledgements

The authors acknowledge financial support from the National Natural Science Foundation of China (grant numbers 61971302).

 

## References


1 D. Huber, A. Oskooei, I. S. X. Casadevall, D. Andrew and G. V. Kaigala, Hydrodynamics in Cell Studies, *Chem. Rev.*, 2018, **118**, 2042–2079.

2 M. P. Stewart, R. Langer and K. F. Jensen, Intracellular Delivery by Membrane Disruption: Mechanisms, Strategies, and Concepts, *Chem. Rev.*, 2018, **118**, 7409–7531.

3 J. Hur and A. J. Chung, Microfluidic and Nanofluidic Intracellular Delivery, *Adv. Sci.*, 2021, **8**, 2004595.

4 A. J. Chung, A Minireview on Inertial Microfluidics Fundamentals: Inertial Particle Focusing and Secondary Flow, *BioChip J.*, 2019, **13**, 53–63.

5 G. Kang, *et al.*, Intracellular Nanomaterial Delivery via Spiral Hydroporation, *ACS Nano*, 2020, **14**, 3048–3058.

6 M. E. Kizer, *et al.*, Hydroporator: a hydrodynamic cell membrane perforator for high-throughput vector-free nanomaterial intracellular delivery and DNA origami biostability evaluation, *Lab Chip*, 2019, **19**, 1747–1754.

7 J. Hur, *et al.*, Microfluidic Cell Stretching for Highly Effective Gene Delivery into Hard-to-Transfect Primary Cells, *ACS Nano*, 2020, **14**, 15094–15106.

8 M. Sun and X. Duan, Recent advances in micro/nanoscale intracellular delivery, *Nanotechnol. Precis. Eng.*, 2020, **3**, 18–31.

9 E. Stride and C. Coussios, Nucleation, mapping and control of cavitation for drug delivery, *Nat. Rev. Phys.*, 2019, **1**, 495–509.

10 A. Yudina, *et al.*, Ultrasound-mediated intracellular drug delivery using microbubbles and temperature-sensitive liposomes, *J. Controlled Release*, 2011, **155**, 442–448.

11 C. McEwan, *et al.*, Combined sonodynamic and antimetabolite therapy for the improved treatment of pancreatic cancer using oxygen loaded microbubbles as a delivery vehicle, *Biomaterials*, 2016, **80**, 20–32.

12 L. Meng, *et al.*, Sonoporation of Cells by a Parallel Stable Cavitation Microbubble Array, *Adv. Sci.*, 2019, **6**, 1900557.

13 P. Marmottant and S. Hilgenfeldt, Controlled vesicle deformation and lysis by single oscillating bubbles, *Nature*, 2003, **423**, 153–156.

14 C. Jia, *et al.*, Generation of reactive oxygen species in heterogeneously sonoporated cells by microbubbles with single-pulse ultrasound, *Ultrasound Interact. Biol. Med.*, 2018, **44**, 1074–1085.

15 J. Rich, Z. Tian and T. J. Huang, Sonoporation: Past, Present, and Future, *Adv. Mater. Technol.*, 2021, **7**, 2100885.

16 A. Salari, *et al.*, Dosage-controlled intracellular delivery mediated by acoustofluidics for lab on a chip applications, *Lab Chip*, 2021, **21**, 1788–1797.

17 M. Thein, *et al.*, Site-specific sonoporation of human melanoma cells at the cellular level using high lateral-resolution ultrasonic micro-transducer arrays, *Biosens. Bioelectron.*, 2011, **27**, 25–33.

18 M. Wu, *et al.*, Acoustofluidic separation of cells and particles, *Microsyst. Nanoeng.*, 2019, **5**, 32.

19 S. Ramesan, *et al.*, Acoustofection: High-Frequency Vibrational Membrane Permeabilization for Intracellular siRNA Delivery into Nonadherent Cells, *ACS Appl. Bio Mater.*, 2021, **4**, 2781–2789.

20 W. Cui, W. Pang, Y. Yang, T. Li and X. Duan, Theoretical and experimental characterizations of gigahertz acoustic streaming in microscale fluids, *Nanotechnol. Precis. Eng.*, 2019, **2**, 15–22.

21 X. Guo, *et al.*, Controllable Cell Deformation Using Acoustic Streaming for Membrane Permeability Modulation, *Adv. Sci.*, 2021, **8**, 2002489.

22 Z. Zhang, *et al.*, Hypersonic Poration: A New Versatile Cell Poration Method to Enhance Cellular Uptake Using a Piezoelectric Nano-Electromechanical Device, *Small*, 2017, **13**, 1602962.

23 S. Pan, T. Jeon, D. C. Luther, X. Duan and V. M. Rotello, Cytosolic Delivery of Functional Proteins In Vitro through Tunable Gigahertz Acoustics, *ACS Appl. Mater. Interfaces*, 2020, **12**, 15823–15829.

24 Y. Lu, *et al.*, Hypersound-Enhanced Intracellular Delivery of Drug-Loaded Mesoporous Silica Nanoparticles in a Non-Endosomal Pathway, *ACS Appl. Mater. Interfaces*, 2019, **11**, 19734–19742.

25 Z. Zhang and Y. Ji, Mesoporous Manganese Dioxide Coated Gold Nanorods as a Multiresponsive Nanoplatform for Drug Delivery, *Ind. Eng. Chem. Res.*, 2019, **58**, 2991–2999.

26 W. Jiang, B. Y. Kim, J. T. Rutka and W. C. Chan, Nanoparticle-mediated cellular response is size-dependent, *Nat. Nanotechnol.*, 2008, **3**, 145–150.

27 X. Huang, S. Neretina and M. A. El-Sayed, Gold Nanorods: From Synthesis and Properties to Biological and Biomedical Applications, *Adv. Mater.*, 2009, **21**, 4880–4910.

28 A. Salvati, *et al.*, Transferrin-functionalized nanoparticles lose their targeting capabilities when a biomolecule corona adsorbs on the surface, *Nat. Nanotechnol.*, 2013, **8**, 137–143.

29 N. Song, *et al.*, Pillar[5]arene–Modified Gold Nanorods as Nanocarriers for Multi–Modal Imaging–Guided Synergistic Photodynamic–Photothermal Therapy, *Adv. Funct. Mater.*, 2021, **31**, 2009924.

30 M. Aioub, S. R. Panikkanvalappi and M. A. El-Sayed, Platinum-Coated Gold Nanorods: Efficient Reactive Oxygen Scavengers That Prevent Oxidative Damage toward Healthy, Untreated Cells during Plasmonic Photothermal Therapy, *ACS Nano*, 2017, **11**, 579–586.

31 C. Xu, *et al.*, Effective Eradication of Tumors by Enhancing Photoacoustic–Imaging–Guided Combined Photothermal Therapy and Ultrasonic Therapy, *Adv. Funct. Mater.*, 2020, **31**, 2009314.

32 P. Armanetti, *et al.*, Enhanced Antitumoral Activity and Photoacoustic Imaging Properties of AuNP–Enriched Endothelial Colony Forming Cells on Melanoma, *Adv. Sci.*, 2020, **8**, 2001175.

33 M. Liu, *et al.*, Real-time visualization of clustering and intracellular transport of gold nanoparticles by correlative imaging, *Nat. Commun.*, 2017, **8**, 15646.

34 Y. Wang, *et al.*, Multistage Adaptive Nanoparticle Overcomes Biological Barriers for Effective Chemotherapy, *Small*, 2021, e2100578.

35 D. Fernando, S. Sulthana and Y. Vasquez, Cellular Uptake and Cytotoxicity of Varying Aspect Ratios of Gold Nanorods in HeLa Cells, *ACS Appl. Bio Mater.*, 2020, **3**, 1374–1384.
36 S. Wang, *et al.*, Hierarchical assembly of gold nanorod stripe patterns for sensing and cells alignment, *Nanotechnology*, 2019, **30**, 175302.
37 Q. Guo, *et al.*, Plasmon mediated spectrally selective and sensitivity-enhanced uncooled near-infrared detector, *J. Colloid Interface Sci.*, 2021, **586**, 67–74.
38 S. He, *et al.*, Ultra-rapid modulation of neurite outgrowth in a gigahertz acoustic streaming system, *Lab Chip*, 2021, **21**, 1948–1955.
39 S. He, *et al.*, Bidirectional Regulation of Cell Mechanical Motion via a Gold Nanorods-Acoustic Streaming System, *ACS Nano*, 2022, **16**, 8427–8439.
40 M. R. K. Ali, *et al.*, Targeting cancer cell integrins using gold nanorods in photothermal therapy inhibits migration through affecting cytoskeletal proteins, *Proc. Natl. Acad. Sci. U. S. A.*, 2017, **114**, E5655–E5663.
41 D. Y. Cho, *et al.*, Triphenylphosphonium-Conjugated Poly (epsilon-caprolactone)-Based Self-Assembled Nanostructures as Nanosized Drugs and Drug Delivery Carriers for Mitochondria-Targeting Synergistic Anticancer Drug Delivery, *Adv. Funct. Mater.*, 2015, **25**, 5479–5491.
42 V. T. Cong, *et al.*, Can the Shape of Nanoparticles Enable the Targeting to Cancer Cells over Healthy Cells?, *Adv. Funct. Mater.*, 2021, 2007880.
43 S. Wilhelm, *et al.*, Analysis of nanoparticle delivery to tumours, *Nat. Rev. Mater.*, 2016, **1**, 16014.
44 H. He, L. Liu, E. E. Morin, M. Liu and A. Schwendeman, Survey of Clinical Translation of Cancer Nanomedicines-Lessons Learned from Successes and Failures, *Acc. Chem. Res.*, 2019, **52**, 2445–2461.
45 Y. Shen, *et al.*, Organelle-Targeting Gold Nanorods for Macromolecular Profiling of Subcellular Organelles and Enhanced Cancer Cell Killing, *ACS Appl. Mater. Interfaces*, 2018, **10**, 7910–7918.
46 L. Zou, *et al.*, Current Approaches of Photothermal Therapy in Treating Cancer Metastasis with Nanotherapeutics, *Theranostics*, 2016, **6**, 762–772.
47 H. Zhao, *et al.*, Microchip based electrochemical-piezoelectric integrated multi-mode sensing system for continuous glucose monitoring, *Sens. Actuators, B*, 2016, **223**, 83–88.